The Astrophysical Journal, 957:23 (9pp), 2023 November 1 https://doi.org/10.3847/1538-4357/acfa02

The Polarized Cosmic Hand: IXPE Observations of PSR B1509−58/MSH 15−5[2]

Roger W. Romani[1], Josephine Wong[1], Niccoló Di Lalla[1], Nicola Omodei[1], Fei Xie[2,3], C.-Y. Ng[4], Riccardo Ferrazzoli[3], Alessandro Di Marco[3], Niccoló Bucciantini[5,6,7], Maura Pilia[8], Patrick Slane[9], Martin C. Weisskopf[10], Simon Johnston[11], Marta Burgay[8], Deng Wei[2], Yi-Jung Yang[12], Shumeng Zhang[4], Lucio A. Antonelli[13,14], Matteo Bachetti[8], Luca Baldini[15,16], Wayne H. Baumgartner[10], Ronaldo Bellazzini[15], Stefano Bianchi[17], Stephen D. Bongiorno[10], Raffaella Bonino[18,19], Alessandro Brez[15], Fiamma Capitanio[3], Simone Castellano[15], Elisabetta Cavazzuti[20], Chien-Ting Chen[21], Nicoló Cibrario[22], Stefano Ciprini[14,23], Enrico Costa[3], Alessandra De Rosa[3], Ettore Del Monte[3], Laura Di Gesu[20], Immacolata Donnarumma[20], Victor Doroshenko[24], Michal Dovčiak[25], Steven R. Ehlert[10], Teruaki Enoto[26], Yuri Evangelista[3], Sergio Fabiani[3], Javier A. Garcia[27], Shuichi Gunji[28], Kiyoshi Hayashida[29], Jeremy Heyl[30], Wataru Iwakiri[31], Ioannis Liodakis[32], Philip Kaaret[10], Vladimir Karas[25], Dawoon E. Kim[3,33,34], Takao Kitaguchi[26], Jeffery J. Kolodziejczak[10], Henric Krawczynski[35], Fabio La Monaca[3], Luca Latronico[18], Grzegorz Madejski[1], Simone Maldera[18], Alberto Manfreda[36], Frédéric Marin[37], Andrea Marinucci[20], Alan P. Marscher[38], Herman L. Marshall[39], Francesco Massaro[18,19], Giorgio Matt[17], Riccardo Middei[13,14], Ikuyuki Mitsuishi[40], Tsunefumi Mizuno[41], Fabio Muleri[3], Michela Negro[42], Stephen L. O'Dell[10], Chiara Oppedisano[18], Luigi Pacciani[3], Alessandro Papitto[13], George G. Pavlov[43], Matteo Perri[13,14], Melissa Pesce-Rollins[15], Pierre-Olivier Petrucci[44], Andrea Possenti[8], Juri Poutanen[45], Simonetta Puccetti[14], Brian D. Ramsey[10], John Rankin[3], Ajay Ratheesh[3], Oliver J. Roberts[21], Carmelo Sgró[15], Paolo Soffitta[3], Gloria Spandre[15], Douglas A. Swartz[21], Toru Tamagawa[26], Fabrizio Tavecchio[46], Roberto Taverna[47], Yuzuru Tawara[40], Allyn F. Tennant[10], Nicholas E. Thomas[10], Francesco Tombesi[23,48,49], Alessio Trois[8], Sergey Tsygankov[45], Roberto Turolla[47,50], Jacco Vink[51], Kinwah Wu[50], and Silvia Zane[50]

[1] Department of Physics and Kavli Institute for Particle Astrophysics and Cosmology, Stanford University, Stanford, CA 94305, USA; rwr@astro.stanford.edu
[2] Guangxi Key Laboratory for Relativistic Astrophysics, School of Physical Science and Technology, Guangxi University, Nanning 530004, People's Republic of China
[3] INAF Istituto di Astrofisica e Planetologia Spaziali, Via del Fosso del Cavaliere 100, I-00133 Roma, Italy
[4] Department of Physics, The University of Hong Kong, Pokfulam, Hong Kong
[5] INAF Osservatorio Astrofisico di Arcetri, Largo Enrico Fermi 5, I-50125 Firenze, Italy
[6] Dipartimento di Fisica e Astronomia, Università degli Studi di Firenze, Via Sansone 1, I-50019 Sesto Fiorentino (FI), Italy
[7] Istituto Nazionale di Fisica Nucleare, Sezione di Firenze, Via Sansone 1, I-50019 Sesto Fiorentino (FI), Italy
[8] INAF Osservatorio Astronomico di Cagliari, Via della Scienza 5, I-09047 Selargius (CA), Italy
[9] Center for Astrophysics | Harvard & Smithsonian, 60 Garden Street, Cambridge, MA 02138, USA
[10] NASA Marshall Space Flight Center, Huntsville, AL 35812, USA
[11] Australia Telescope National Facility, CSIRO, Space and Astronomy, P.O. Box 76, Epping NSW 1710, Australia
[12] Department of Physics & Laboratory for Space Research, The University of Hong Kong, Pokfulam, Hong Kong
[13] INAF Osservatorio Astronomico di Roma, Via Frascati 33, I-00078 Monte Porzio Catone (RM), Italy
[14] Space Science Data Center, Agenzia Spaziale Italiana, Via del Politecnico snc, I-00133 Roma, Italy
[15] Istituto Nazionale di Fisica Nucleare, Sezione di Pisa, Largo B. Pontecorvo 3, I-56127 Pisa, Italy
[16] Dipartimento di Fisica, Università di Pisa, Largo B. Pontecorvo 3, I-56127 Pisa, Italy
[17] Dipartimento di Matematica e Fisica, Università degli Studi Roma Tre, Via della Vasca Navale 84, I-00146 Roma, Italy
[18] Istituto Nazionale di Fisica Nucleare, Sezione di Torino, Via Pietro Giuria 1, I-10125 Torino, Italy
[19] Dipartimento di Fisica, Università degli Studi di Torino, Via Pietro Giuria 1, I-10125 Torino, Italy
[20] ASI—Agenzia Spaziale Italiana, Via del Politecnico snc, I-00133 Roma, Italy
[21] Science and Technology Institute, Universities Space Research Association, Huntsville, AL 35805, USA
[22] Dipartimento di Fisica, Universitá degli Studi di Torino, Via Pietro Giuria 1, I-10125 Torino, Italy
[23] Istituto Nazionale di Fisica Nucleare, Sezione di Roma "Tor Vergata," Via della Ricerca Scientifica 1, I-00133 Roma, Italy
[24] Institut für Astronomie und Astrophysik, Universität Tübingen, Sand 1, D-72076 Tübingen, Germany
[25] Astronomical Institute of the Czech Academy of Sciences, Boční II 1401/1, 14100 Praha 4, Czech Republic
[26] RIKEN Cluster for Pioneering Research, 2-1 Hirosawa, Wako, Saitama 351-0198, Japan
[27] California Institute of Technology, Pasadena, CA 91125, USA
[28] Yamagata University,1-4-12 Kojirakawa-machi, Yamagata-shi 990-8560, Japan
[29] Osaka University, 1-1 Yamadaoka, Suita, Osaka 565-0871, Japan
[30] University of British Columbia, Vancouver, BC V6T 1Z4, Canada
[31] International Center for Hadron Astrophysics, Chiba University, Chiba 263-8522, Japan
[32] Finnish Centre for Astronomy with ESO, 20014 University of Turku, Finland
[33] Dipartimento di Fisica, Universitá degli Studi di Roma "La Sapienza," Piazzale Aldo Moro 5, I-00185 Roma, Italy
[34] Dipartimento di Fisica, Universitá degli Studi di Roma "Tor Vergata," Via della Ricerca Scientifica 1, I-00133 Roma, Italy
[35] Physics Department and McDonnell Center for the Space Sciences, Washington University in St. Louis, St. Louis, MO 63130, USA
[36] Istituto Nazionale di Fisica Nucleare, Sezione di Napoli, Strada Comunale Cinthia, I-80126 Napoli, Italy
[37] Université de Strasbourg, CNRS, Observatoire Astronomique de Strasbourg, UMR 7550, F-67000 Strasbourg, France
[38] Institute for Astrophysical Research, Boston University, 725 Commonwealth Avenue, Boston, MA 02215, USA
[39] MIT Kavli Institute for Astrophysics and Space Research, Massachusetts Institute of Technology, 77 Massachusetts Avenue, Cambridge, MA 02139, USA
[40] Graduate School of Science, Division of Particle and Astrophysical Science, Nagoya University, Furo-cho, Chikusa-ku, Nagoya, Aichi 464-8602, Japan
[41] Hiroshima Astrophysical Science Center, Hiroshima University, 1-3-1 Kagamiyama, Higashi-Hiroshima, Hiroshima 739-8526, Japan
[42] Department of Physics and Astronomy, Louisiana State University, Baton Rouge, LA 70803 USA
[43] Department of Astronomy and Astrophysics, Pennsylvania State University, University Park, PA 16802, USA
[44] Université Grenoble Alpes, CNRS, IPAG, F-38000 Grenoble, France
[45] Department of Physics and Astronomy, University of Turku, FI-20014, Finland

[46] INAF Osservatorio Astronomico di Brera, Via E. Bianchi 46, I-23807 Merate (LC), Italy
[47] Dipartimento di Fisica e Astronomia, Università degli Studi di Padova, Via Marzolo 8, I-35131 Padova, Italy
[48] Dipartimento di Fisica, Università degli Studi di Roma "Tor Vergata," Via della Ricerca Scientifica 1, I-00133 Roma, Italy
[49] Department of Astronomy, University of Maryland, College Park, MD 20742, USA
[50] Mullard Space Science Laboratory, University College London, Holmbury St Mary, Dorking, Surrey RH5 6NT, UK
[51] Anton Pannekoek Institute for Astronomy & GRAPPA, University of Amsterdam, Science Park 904, 1098 XH Amsterdam, The Netherlands
Received 2023 July 31; revised 2023 September 12; accepted 2023 September 13; published 2023 October 23

Abstract

We describe IXPE polarization observations of the pulsar wind nebula (PWN) MSH 15−5^2, the "Cosmic Hand." We find X-ray polarization across the PWN, with *B*-field vectors generally aligned with filamentary X-ray structures. High-significance polarization is seen in arcs surrounding the pulsar and toward the end of the "jet," with polarization degree PD > 70%, thus approaching the maximum allowed synchrotron value. In contrast, the base of the jet has lower polarization, indicating a complex magnetic field at significant angle to the jet axis. We also detect significant polarization from PSR B1509−58 itself. Although only the central pulse phase bin of the pulse has high individual significance, flanking bins provide lower-significance detections and, in conjunction with the X-ray image and radio polarization, can be used to constrain rotating vector model solutions for the pulsar geometry.

Unified Astronomy Thesaurus concepts: Pulsar wind nebulae (2215); Rotation powered pulsars (1408); Polarimetry (1278)

Supporting material: data behind figure

1. Introduction

PSR B1509−58 (=PSR J1513−5809) is a young ($\tau =$ 1600 yr), energetic ($\dot{E} = 1.7 \times 10^{37}$erg s^{-1}), high-field ($B_s =$ 1.5×10^{13} G) pulsar embedded in the supernova remnant (SNR) RCW 89/G320.4−1.2/MSH 15−5^2 (Caswell et al. 1981). The relativistic particles and fields produced by this pulsar power a bright X-ray pulsar wind nebula (PWN), whose spectacular Chandra X-ray Observatory (CXO) image has earned the moniker the "Cosmic Hand" or the "Hand of God." This structure and the surrounding SNR are detected from radio (Leung & Ng 2016) to TeV (Aharonian et al. 2005) energies with complex morphology, often complementary at different energy bands. At a distance $d \approx 5$ kpc the 32′-diameter radio shell spans 47 pc. The PWN's nonthermal X-ray emission extends ∼8′ from the pulsar, making the PWN complex ∼4 × larger in angle and ∼10 × larger in size than the famous Crab PWN. MSH 15−5^2 shares a "torus+ jet" morphology with the Crab, with a ∼10″ subluminous X-ray zone around the pulsar representing the pre-termination shock flow (Yatsu et al. 2009). The two bright X-ray arcs wrapping the northern side of the pulsar may represent the distorted equatorial torus of the shocked PWN or may represent field lines wrapped around the termination shock by ram pressure or backflow in the surrounding PWN (Figure 1). To the south along the torus axis is a prominent ridge of X-ray emission extending at least 5′, often referred to as a "jet" (Gaensler et al. 2002). To the northwest, nonthermal X-ray ridges form the "thumb" and "fingers" of the hand. The fingers extend to a region of softer thermal X-ray emission to the north.

The $P_s = 150$ ms pulsations are detected in the radio (Manchester et al. 1982), X-ray (Seward & Harnden 1982), and γ-ray (Abdo et al. 2010) bands. The pulsed spectral energy distribution (SED) is actually quite soft for a γ-ray pulsar, peaking at ∼10 MeV, which may be associated with its relatively large dipole field. As for most young gamma-ray pulsars, the high-energy emission lags the radio peak, here by $\Delta\phi \approx 0.3$. At X-ray energies, the peak has two overlapping peaks, with separation $\delta\phi \approx 0.2$ (de Plaa et al. 2003).

Existing polarization information on this system is limited. While the supernova shell itself is quite bright in the radio, the nonthermal emission is radio-faint. Radio observations with the Australia Telescope Compact Array (ATCA) at 3 and 6 cm have detected significant linear polarization, especially in the torus-like arcs (Leung & Ng 2016; S. Zhang et al. 2023, in preparation). Here the inferred magnetic field follows the arcs as they wrap around the pulsar. To the south, this polarized radio emission brackets the X-ray jet. The X-ray jet fills a cavity in the radio emission, with little or no radio flux apparent, as also noted by Gaensler et al. (2002). To the north, radio emission seems to follow the thumb and finger structures but is rather faint for reliable polarization maps. Like many young energetic pulsars, B1509–58 shows high linear polarization in the radio (Crawford et al. (2001; Rookyard et al. (2015a). From the ROSAT X-ray PWN structure Brazier & Becker (1997) qualitatively estimated the viewing angle $i > 70°$, although a somewhat smaller value is indicated by CXO data (Figure 3). There is a claim of a pulsar-phase-averaged optical polarization of degree PD ∼ 10.4% by Wagner & Seifert (2000), but the measurement is compromised by a bright field star, and lacking any error bar or position angle (PA) estimate, this measurement needs to be confirmed.

Here we report on the first measurements of X-ray polarization from this complex, with robust detections of both the pulsar and the surrounding PWN, and describe how these results constrain the system geometry.

2. IXPE Observations of PSR B1509−58/MSH 15−5^2

The Imaging X-ray Polarimetry Explorer (IXPE), the first mission devoted to spatially resolved polarization measurements in X-rays (Weisskopf et al. 2022), was successfully launched on 2001 December 9. IXPE observed MSH 15−5^2 on 2022 September 2–16, 2023 February 14–21, and 2023 March 13–19 for a total of ∼1.5 Ms live time. Data were extracted and analyzed according to standard procedures: `HEASOFT` 6.30.1 (NASA High Energy Astrophysics Science Archive Research

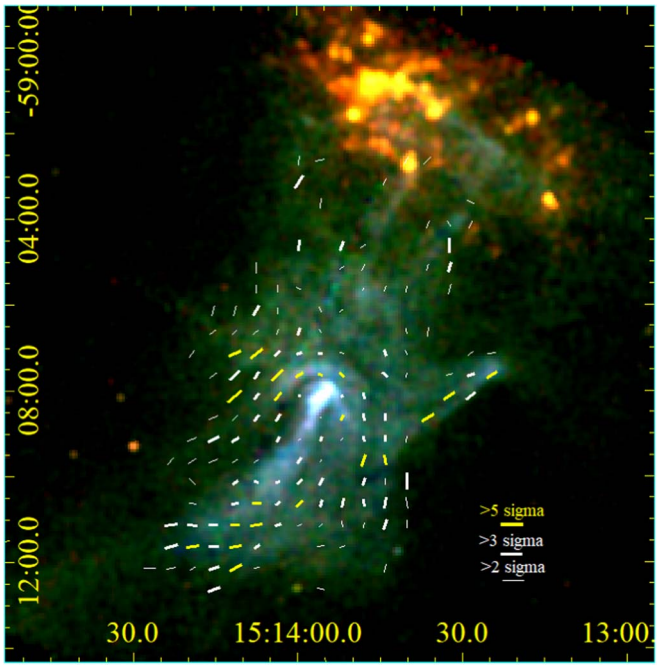

Figure 1. Overview of the MSH 15−5[2] complex, the "Cosmic Hand." The background energy-coded CXO image (0.5–1.2 keV = red, 1.2–2 keV = green, 2–7 keV = blue) shows low-energy (red/yellow) emission from thermal gas in G320.4−1.2 and harder nonthermal emission from the PWN. Superposed are IXPE 2–8 keV PCUBE-derived bars showing the polarization degree (PD, bar length in the legend is for PD = 1) and projected magnetic field direction on a 30″ grid. Yellow bars show >5σ polarization detections, thick white bars >3σ, and thin white bars >2σ. In general, the magnetic field appears to follow the thumb, fingers, and other linear structures (see Figure 2 for region labels). Particularly strong polarization is associated with the arc, especially to the northeast of the pulsar and with the far southeast end of the jet. We have used a flux cut to trim anomalous vectors near the field-of-view edge.

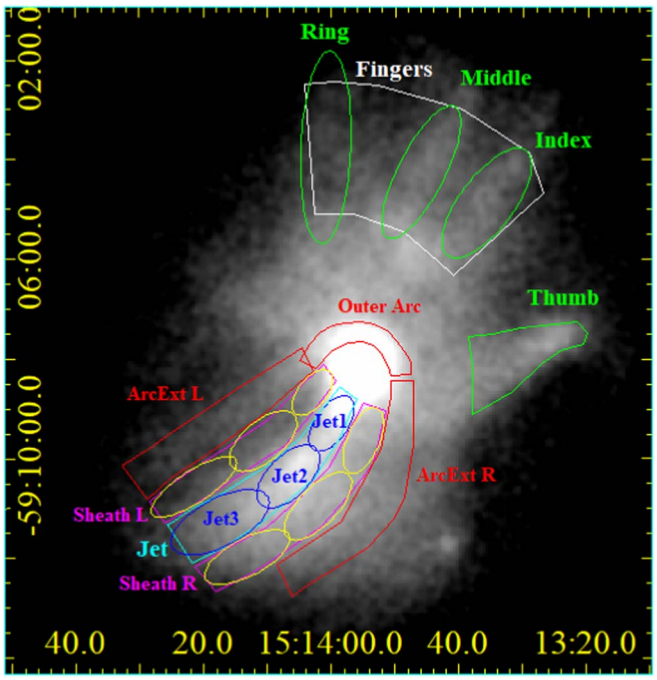

Figure 2. Morphological regions of interest on the IXPE combined DU1-3 2–8 keV image. The Hand's "wrist" includes the bright jet and flanking filament structures, divided here into several regions.

Center (HEASARC), 2014) was used to perform barycenter corrections using the DE421 JPL ephemeris. ixpeobssim V30.2.2 (Baldini et al. 2022) was used to do energy calibration, detector WCS correction, bad aspect ratio corrections, and all further analysis, including phase folding at the pulsar ephemeris.

Background events were cleaned from the data following the procedure of Di Marco et al. (2023). The residual instrumental background was modeled from 1.5 Ms of cleaned IXPE source-free exposure in the fields of several high-latitude sources (MGC-5-23-16, 1ES 0299+200, PG 1553, PSR B0540−69, and IC 4329A). MSH 15−5[2] lies close to the Galactic ridge, so some contribution from background X-rays is expected as well. However, it covers most of the IXPE field of view, so we cannot extract a local background spectrum directly from IXPE. Instead, we use CXO observations to compute the background flux, passed through the IXPE instrument response, south of the thumb, finding a count rate ∼1.1 × the instrumental background, and so we increase the background spectrum surface brightness by this factor. This unpolarized background surface brightness (8.9×10^{-8}counts arcsec^{-2} s^{-1} det^{-1}, 2–5.5 keV; 1.07×10^{-7} counts arcsec^{-2} s^{-1} det^{-1}, 2–8 keV) is scaled and subtracted from the flux of each aperture.

Since DeLaney et al. (2006) have noted temporal variations in the fine structure of the PWN, especially in knots near the pulsar but also in the jet feature, we collected a contemporaneous 28 ks CXO observation of the PWN (ObsIDs 23540, 27448) to have a current high-resolution image for comparison.

Figure 1 gives an overview of the IXPE polarization measurements superimposed on an energy-coded image from archival CXO exposures (ObsIDs 0754, 3833, 5534, 5535, 6116, 6117—204 ks live time total). Here we show the projected magnetic field direction (orthogonal to the electric vector position angle (EVPA)) measured on a 30″ grid, comparable to the resolution of the IXPE point-spread function (PSF). Complex polarization features extend throughout the nebula.

We can use the deep archival data to define nebula regions of interest (Figure 2 and Table 2). This allows us to discuss the polarization properties of extended regions too faint for high signal-to-noise ratio mapping. The 2022 CXO image does show small departures from the archival morphology; most are changes in the shock structure near the pulsar, within the central IXPE resolution element, although there are also small changes in the jet 1′–2′ from the pulsar. None affect the locations of our extended regions. In the region near the pulsar, CXO maps show an inner arc, not resolved by IXPE (Figure 3). Strong, high-significance polarization follows the outer arc, as also seen in the 6 cm radio maps. The arc magnetic field structure extends, with field lines parallel to the jet, in left and right "arc extensions." It is more faintly visible in the sheath regions flanking the X-ray-bright jet. The field also clearly follows the curve of the thumb region. All of these features are also discernible in the radio. In addition, we measure fields paralleling the "finger" structures—in the radio, these are lost to bright emission from shock in the SNR shell. The shell interaction produces the low-energy X-ray emission appearing in red and yellow to the north in Figure 1. This thermal emission, near the edge of the IXPE field of view, is unpolarized.

The general pattern of polarization in Figure 1 is as expected, with the magnetic field lines following the filamentary nebula structure. The highest fractional polarizations, in the outer arc, thumb, and end of the jet, reach PD ∼ 70% (after background subtraction). By integrating over the regions of Figure 2, we

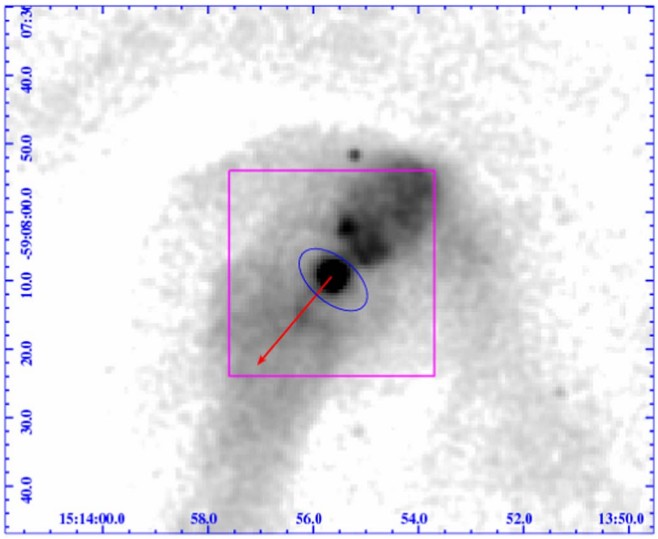

Figure 3. Inner region of MSH 15−5[2] from 0.5–8 keV CXO data, centered on the pulsar and smoothed with a 1″ Gaussian kernel. Note the subluminous zone (marked by an ellipse 2/3 of the zone size), the symmetry axis (red arrow), the bright polar outflow to the northwest, and the fainter, more diffuse outflow to the southeast. The magenta square marks the central pixel of the PCUBE polarization map, Figure 1 (approximating IXPE's resolution); "simultaneous fit" pixels are half this size, Figure 4. The "Inner Arc" passes through the northwest polar outflow, while the "Outer Arc" is partly visible to the north.

also see that the magnetic field is aligned with the thin "finger" structures, but with substantial background from the thermal emission at the fingertips, we suspect that the PD in these regions is underestimated.

The most unusual feature is the X-ray-bright hard spectrum "jet," which is essentially invisible in the radio, implying a low-energy cutoff in the jet electron spectrum. This may be an intrinsic cutoff in the injected electron spectrum or the result of limited time available for cooling in the rapid jet flow. We also note that the overall polarization level is low at the base of the jet region. Interestingly, the weak polarization that we do see appears to be at a substantial angle to that of the bracketing nebula. These are, of course, 3D structures, so it seems likely that the jet zone is viewed through a plasma emitting like the "sheath" zones to either side. If we subtract the average Stokes I, Q, and U of this sheath (scaled for area), we do indeed see jet polarization increase to PD $> 60\%$, with the measured EVPA implying an average magnetic field at angles up to 50° from the jet axis.

3. Phase-resolved Analysis of PSR B1509−58

We obtained contemporaneous Parkes L-band radio observations (2023 2/7, 2/20, 2/26, and 3/1) and folded them with the same ephemeris used for the IXPE X-ray events to confirm that the $\Delta\phi = 0.25$ radio−X-ray phase lag (Kawai et al. 1991; Cusumano et al. 2001) remains valid.

To extract the nebula map and the pulsar polarization, we employ the "Simultaneous Fitting" technique of Wong et al. (2023). This uses the contemporaneous 2022 CXO image of the nebula, with the point source subtracted, to define the intensity (and local spectrum) of the extended emission at the IXPE observation epoch. For the pulsar point-source contribution, we also rely on CXO data, using the ACIS-CC and HRC analysis of Hu et al. (2017) to define the light curve and phase-varying spectral index of the pulsar emission. The phase-dependent pulsar and spatially dependent nebula spectra are folded through the IXPE response, using `ixpeobsim`, to predict the IXPE counts as a function of position and phase. Note that PSR B1509−58 is relatively bright at minimum, at ∼4% of its peak flux—this means that the phase-invariant DC emission contributes ∼11% of the pulsed flux. To model faint PWN regions, the uniform background must be included in the simultaneous fitting model; here we use the instrumental background, as local photon background is included in the CXO-derived flux.

Simultaneous fitting defines a set of spatial and phase bins and uses the predicted IXPE counts from the nebula, background, and PSF-distributed pulsar to define the expected PSR/PWN contributions to each bin. It then executes a global least-squares fit for the pulsar polarization at each phase and the phase-independent nebular polarization at each spatial pixel. Here we define a 13×11, 15″-pixel grid centered on the pulsar. We use 2–5.5 keV photons to best isolate the pulsar polarization signal (which is slightly softer than the spectrum of the inner PWN) and simple "Moments Ellipticity" weights to quantify the accuracy of the polarization reconstruction of each event. Note that with different PSFs for each detector (as measured from ground calibration images) and different spacecraft orientations for each of the three IXPE pointings, we have nine measurements of the combined PSR/PWN polarization signal in each spatial and phase bin, all of which must be simultaneously fit.

Because errors in the reconstructed photon conversion point are correlated with the reconstructed polarization vector, bright point sources (and any sharp flux gradient) will have a "halo" of polarization at scales less than the PSF FWHM, which can be corrected by an iterative estimate of this so-called polarization leakage (Bucciantini et al. 2023). Here we apply the energy-dependent version of this correction, using the detailed ground-measured PSFs of the three telescope assemblies, as outlined in Wong et al. (2023). This correction is applied before the simultaneous fit extraction of the component polarizations. The correction makes modest (<20%) amendments to the polarization degree in the inner few arcminutes, especially associated with the relatively sharp arcs to the north of the pulsar. In addition, when the spatial bins are smaller than the PSF FWHM and the counts per bin are low, anticorrelated fluctuations between adjacent pixels increase the scatter and error in fit q and u. Here we mitigated this by smoothing the q and u maps by the PSFs for a decrease in fluctuations, at a cost of some spatial resolution.

In Figure 5 we show the simultaneous fitting-derived pulsar X-ray EVPA estimates along with radio polarization measurements and the IXPE X-ray light curve for reference. Only one X-ray phase bin, near the center of the peak, is significant with a PD of 17.5% at 3.7σ. The large pulse-minimum bin formally has a very high PD ∼ 1 at low significance. However, the PCUBE analysis shows small total polarization in the central pixel—simultaneous fitting evidently optimizes the central region fit by introducing some q and u into the faint minimum phase pulsar component and producing canceling PSR minimum and PWN polarizations in this phase bin. The other bins in the X-ray peak have low PD = 10%–20%; at ∼2σ–3σ significance per bin there is no definitive polarization detection, although the EVPA values do assume an intriguing smooth sweep across the X-ray peak.

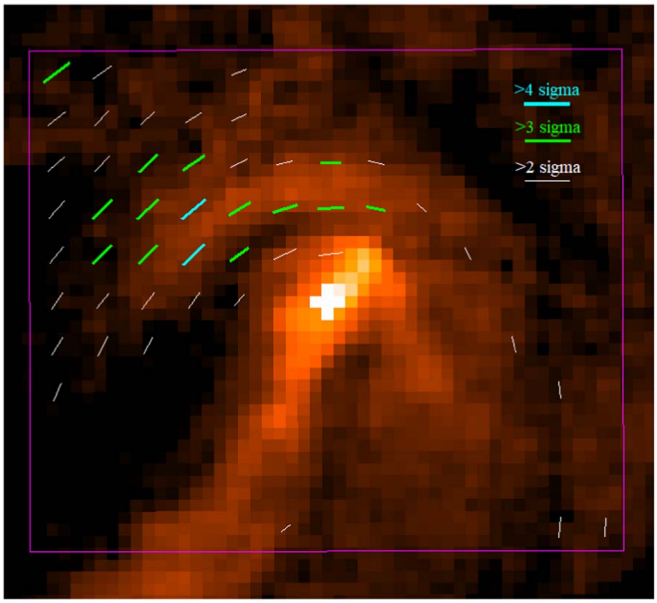

Figure 4. 2–5.5 keV polarization bars (orthogonal to the EVPA), as determined from simultaneous fitting inside the magenta region (cyan bars $>4\sigma$ significance, green bars $>3\sigma$, white bars $>2\sigma$; the labels at upper right show the bar length for PD = 1). Here we employ a 15″ grid to better resolve the pulsar from inner nebula structures. Background is the full-band CXO image.

4. Discussion

The background-subtracted, leakage-corrected polarization map (Figure 1) has several $>5\sigma$ polarization regions. The most significant (left arc extension) pixel has a background-subtracted PD $= 0.72 \pm 0.08$. A few low-count pixels near the nebula edge have higher PD, the most extreme being in the left arc extension, with PD $= 0.87 \pm 0.14$. Thus, all pixels are consistent with PD < 0.75 at the 1σ level. Other highly polarized pixels are at the jet end (PD $= 0.65 \pm 0.12$), the thumb base (PD $= 0.66 \pm 0.11$), and the index finger (PD $= 0.73 \pm 0.20$). The jet as a region is highly polarized toward its end with PD $= 0.83 \pm 0.16$ at its far (J3) end, if one subtracts the adjacent sheath emission as a background. Thus, as also seen in the Vela PWN (Xie et al. 2022), polarization approaches PD $= \Gamma_X/(\Gamma_X + 2/3)$, the maximum allowed for synchrotron polarization at the observed X-ray photon index Γ_X in a uniform magnetic field. For example, in the J3-Sh3 region, the maximum allowed value is PD $= 0.72$; the observed polarization is 0.7σ above this value, consistent with a statistical fluctuation.

In the inner region, simultaneous fitting lets us map fields closer to the pulsar (Figure 4). Here again the strongest polarization follows the outer arc and the left arc extension, with a peak value of PD $= 0.64 \pm 0.14$. There is also a PD $= 0.54 \pm 0.19$ polarized pixel of modest 2.8σ significance located on the ridge of the inner arc. This should be a pure nebula measurement, as it comes from the nebula portion of the simultaneous fit, generated with the contemporaneous CXO-defined structure, and has also been corrected for polarization leakage. However, at only 15″ from the pulsar PSF peak, some concern about systematic effects persists. At both scales, polarization at the base of the jet is low.

Table 2 lists the average polarization degree and angle in the larger regions defined in Figure 2. We can estimate the regions' magnetic field strength under the assumption of equipartition. For an optically thin region filled with relativistic electrons and magnetic field emitting synchrotron radiation the equipartition field is

$$B_{\rm Eq} = 46\left[\frac{J_{-20}(E_1, E_2)\sigma}{\phi}\frac{C_{1.5-\Gamma}(E_m, E_M)}{C_{2-\Gamma}(E_1, E_2)}\right]^{2/7}\mu G, \quad (1)$$

where

$$C_q(x_1, x_2) = \frac{x_2^q - x_1^q}{q}. \quad (2)$$

$J_{-20}(E_1, E_2) = 4\pi f_X(E_1, E_2)d^2/V$ is the observed emissivity (in 10^{-20} erg s^{-1} cm^{-3}, between E_1 keV and E_2 keV), $\sigma_B = w_B/w_e$ is the magnetization parameter, ϕ is the filling factor, and E_m and E_M are the minimum and maximum energies, in keV, of the synchrotron spectrum with photon index Γ. We assume that the structures are cylindrical, with diameter set to the observed region width. We list the derived equipartition fields in Table 1 for $\sigma = \phi = 1$, $E_m = 0.01$ keV, and $E_M = 10$ keV.

MSH 15−5[2] is complex, but a few trends can be extracted from Table 1. First, the fingers region is notably softer than the bulk of the PWN. This may, in part, be due to contamination by the soft thermal emission to the north. However, the "thumb" with $\Gamma = 1.92$ is free of the thermal emission but still somewhat softer than the outer arc. The hardest feature is, of course, the "jet" as seen in the color image (Figure 1). This suggests that this feature contains the freshest electron population and that the outer features have suffered some synchrotron burn-off. Indeed, the jet may represent a site of $e^{\pm}$ reacceleration, and the low polarization at its base may be, in part, due to magnetic turbulence and dissipation there. The spectral trends are broadly consistent with those found by An et al. (2014). These authors, using NuSTAR, infer a nebula-averaged spectral break at ∼6 keV. Thus, the average CXO spectral indices shown here should not resolve a full $\Delta\Gamma = 0.5$ cooling break.

Our equipartition field estimates are, of course, subject to the uncertain 3D geometry and ϕ fill factor. There does seem to be a trend of higher fields to the north, which may be associated with compression from interaction with G320.4−1.2. We also note that the equipartition field strength appears to decrease along the jet, although the field becomes more uniform, as shown by the PD increase as one moves away from the pulsar.

The field orientations for the morphological regions support the pattern in Figure 1, with the arc and thumb fields well aligned with the curved ridges. The mean "jet" field is oriented ∼25°–35° from the surrounding "sheath" regions. If we imagine that these are 3D structures, with the sheath surrounding the jet, we can subtract the mean sheath flux, to find that the offset angle increases to ∼40°–50° and the residual polarization is quite high at PD $= 62\% \pm 8\%$. The jet field is not fully transverse to the jet axis, but the significant orthogonal component might implicate a helical structure. We subdivided the jet into three regions, finding a strongly increasing polarization as one moves downstream. The B orientations do not show a smooth trend, even after subtracting flanking sheath fluxes. The brightest mid-jet region, however, has the largest angle to the local jet axis at ≈50°.

Pulsar polarization can also be related to the PWN geometry. Examining the CXO-measured fine structure in the inner nebula, we see a general symmetry axis at $\psi = 140° \pm 5°$. PWN features are best described by tangential views of structure in the MHD flow, as described by Komissarov & Lyubarsky (2003), but the geometrical inferences from a torus–

Table 1
CXO Spectral Measurements and IXPE PCUBE Polarizations for the Regions of Figure 2

Region	Flux (0.5–8 keV)	Γ_X	B_{Eq} (μG)	Q	U	Q, U err	PD	ψ (deg)	Sig
Fingers	26.98	2.35 ± 0.01	21	-0.119	0.114	0.022	0.165 ± 0.022	68.0 ± 3.8	7.5
Index	5.64	2.22 ± 0.01	24	-0.216	0.065	0.044	0.225 ± 0.044	81.7 ± 5.6	5.1
Middle	6.65	2.34 ± 0.01	29	-0.055	0.183	0.043	0.191 ± 0.043	53.3 ± 6.5	4.4
Ring	4.95	2.26 ± 0.02	22	-0.177	0.121	0.050	0.214 ± 0.050	72.8 ± 6.7	4.3
Thumb[b]	6.15	1.92 ± 0.01	16	0.313	-0.085	0.038	0.324 ± 0.038	-7.6 ± 3.4	8.4
Outer arc[b]	6.38	1.87 ± 0.01	27	0.348	-0.020	0.026	0.348 ± 0.026	-1.7 ± 2.1	13.5
ArcExt L	4.10	1.93 ± 0.01	22	0.084	0.412	0.043	0.421 ± 0.043	39.2 ± 2.9	9.7
ArcExt R	9.12	1.84 ± 0.01	16	-0.109	0.075	0.027	0.133 ± 0.027	72.7 ± 5.9	4.9
Jet	15.81	1.69 ± 0.01	18	0.238	0.089	0.021	0.254 ± 0.021	10.2 ± 2.3	12.2
Sheath L	3.47	1.77 ± 0.02	16	-0.001	0.142	0.034	0.142 ± 0.034	45.2 ± 6.9	4.2
Sheath R	9.68	1.80 ± 0.01	20	0.092	0.256	0.025	0.272 ± 0.025	35.1 ± 2.6	11.0
Jet-sheath[a]				0.602	-0.146	0.075	0.620 ± 0.075	-6.8 ± 3.4	8.3
J1	4.58	1.64 ± 0.01	25	0.012	0.173	0.037	0.173 ± 0.037	43.1 ± 6.1	4.7
J2	6.54	1.74 ± 0.01	19	0.276	0.034	0.035	0.278 ± 0.035	3.5 ± 3.6	8.0
J3	4.59	1.67 ± 0.01	16	0.466	0.053	0.041	0.469 ± 0.041	3.2 ± 2.5	11.5
J1-Sh1[a]				0.281	0.123	0.109	0.307 ± 0.109	11.8 ± 10.1	2.8
J2-Sh2[a]				0.526	-0.293	0.090	0.602 ± 0.090	-14.6 ± 4.3	6.7
J3-Sh3[a]				0.819	-0.145	0.159	0.831 ± 0.159	-5.0 ± 5.3	5.2

Notes. Γ_X—photon index; 0.3–8 keV unabsorbed fluxes in 10^{-12} erg cm^{-2} s^{-1} (spectral fits include a common PhAbs model $N_H = 8.96 \pm 0.04 \times 10^{21}$ cm^{-2} absorption); equiparttition fields are for $\sigma = \phi = 1$. PD—polarization fraction; ψ—EVPA.
[a] Average of flanking background subtracted for jet and jet subregions.
[b] (Outer arc, thumb) polarization measured along an arc; $\psi = 0°$ represents a B field oriented along the arc.

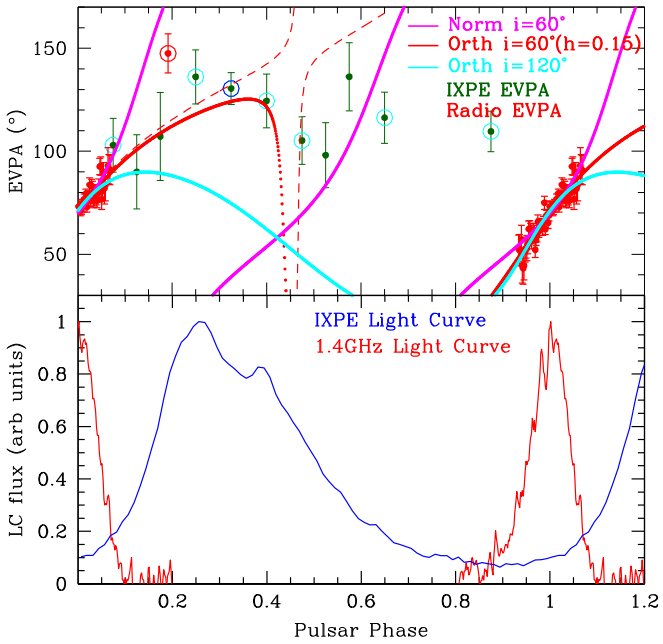

Figure 5. Top: IXPE phase bin PA estimates (green; q and u values available as data behind figure). The blue circled bin at pulse center is individually significant (3.7σ); cyan circled points are at 2σ–3σ. The radio PAs (red) can be fit (excluding the circled point) with the normal mode (magenta) and orthogonal mode (red) $i \sim 60°$ models. For the $i \sim 120°$ model only the orthogonal mode solution is tenable. Note that the $i \sim 60°$ models better accommodate the late radio point and the X-ray data. A somewhat better match can be found for the orthogonal mode model when the X-ray emission is at higher altitude, with modest altitude h (dashed curve). Bottom: IXPE pulsar light curve (blue), Parkes 1.4 GHz light curve (red).
(The data used to create this figure are available.)

jet picture with cylindrical symmetry are robust. As for the Crab, there is a subluminous zone surrounding the pulsar, first described for MSH 15−5^2 by Yatsu et al. (2009), which marks the equatorial flow prior to the termination shock (marked in Figure 3 by an ellipse). For the Crab this zone is bracketed by the inner ring and wisps. The Crab wisps are brighter to the northwest, and if interpreted as due to Doppler boosting in mildly relativistic post-shock flow (Ng & Romani 2008), this determines the 3D orientation of the spin axis. For MSH 15−5^2 the zone has no bright edge and the Doppler boosting is not obvious. So while the ellipticity of the zone constrains the spin axis inclination to the Earth line of sight, both $i = 60° \pm 2°$ with the southeast axis out of the plane of the sky (since the "jet" to the southeast would then approach us, we call this the "jet" solution) and $i = 120° \pm 2°$ with that axis into the plane of the sky (the "C-jet" solution) are viable. One might interpret the blob of polar emission to the northwest in Figure 3 as a Doppler boosted "jet." However, it is diffuse and is more likely outflow analogous to the dome of PWN emission northwest of the Crab, rather than a collimated relativistic jet flow.

We can compare this geometry with that inferred from radio pulsar polarization measurements. Figure 5 shows Parkes 1.4 GHz EVPA values, referenced to infinite frequency for a rotation measure of RM = 216.0 rad m^{-2} (Johnston & Weisberg 2006), where phase bins with linear polarization detected with $>2.5\sigma$ significance are plotted. Traditionally one fits the EVPA data $\psi(\phi)$ to the rotating vector model (RVM; Radhakrishnan & Cooke 1969), which can be generalized to include the effect of Doppler boosting of the rotating emission point at height $h = r/R_{LC}$ as (e.g., Poutanen 2020)

$$\tan(\psi - \psi_0) = \frac{\sin\theta \sin(\phi - \phi_0) + h[\sin i \sin\theta + \cos i \cos\theta \cos(\phi - \phi_0)]}{\cos i \sin\theta \cos(\phi - \phi_0) - \sin i \cos\theta - h \cos\theta \sin(\phi - \phi_0)},$$

where $h \approx 0$ for the low-altitude radio emission. Here i is the inclination of the spin axis to the line of sight, θ is the angle between the magnetic and spin axes, and the magnetic axis passes closest to the line of sight at $\phi = \phi_0$ with impact

Table 2
MCMC Radio RVM Fits—see Figure 5

Parameter	Norm Jet	Orth Jet	Orth C-Jet
i (deg)	58.0 ± 1.9	60.0 ± 1.9	119.7 ± 2.0
θ (deg)	87.6 ± 3.8	123.0 ± 2.7	148.5 ± 1.6
ϕ_0 (deg)	48.9 ± 3.3	-22.6 ± 3.0	-18.1 ± 2.4
Ψ_0 (deg)	138.1 ± 2.7	49.9 ± 2.9	52.8 ± 2.7
β (deg)	-28.7	-63.0	-28.8
$\chi^2/63$ dof	1.37	1.13	1.19

Note. Priors from X-ray (Figure 3)—$\psi_0 = 140^\circ \pm 3^\circ$ (norm), $50^\circ \pm 3^\circ$ (orth), $i = 60^\circ \pm 2^\circ$ (jet), $i = 120^\circ \pm 2^\circ$ (C-jet).

parameter $\beta = i - \theta$ and EVPA ψ_0. Note that the sign of the denominator addresses the "ψ convention problem" (Everett & Weisberg 2001). With the limited radio phase coverage, a simple $h = 0$ fit to the radio data is not particularly constraining (Rookyard et al. 2015b), but if we impose the prior constraints on ψ_0 (which is either along or orthogonal to the projected spin axis at phase ϕ_0; Johnston et al. 2005) and i (two options, above) from the X-ray image, we obtain fits with well-constrained parameters and small covariance. In Table 2 we show the Markov Chain Monte Carlo fit parameters for the three viable options (the normal mode orientation with $i \approx 120^\circ$ provides no acceptable fit to the radio data). Both orthogonal mode solutions provide very good fits. The one normal mode solution is worse but, with a p-value of 0.025, still acceptable. If the X-ray image constraints are relaxed, the best-fit solutions remain stable, although errors, of course, increase and there is substantial $\phi_0 - \psi_0$ covariance.

The IXPE polarization data (and the late-phase radio point) can help us distinguish between RVM models. The $i \approx 120^\circ$ RVM model cannot explain these points, as the model EVPA is far off. The $i \approx 60^\circ$ models have EVPA increasing past the radio peak and so more plausibly account for these data. In fact, for these models the post-radio EVPA increases slightly for higher-altitude emission; the orthogonal $i \approx 60^\circ$ model can match the IXPE EVPA and approach the late-phase radio point if their emission is from higher altitude with $h > 0$. A fit to the X-ray data formally gives $h \approx 0.15 \pm 0.05$, but there are multiple minima and large departures at late phases. Note that the $i \approx 60^\circ$ orthogonal model sweep is slowest near the significant IXPE detection. For this case some loss of polarization signal might be attributed to sweep in the surrounding bins. Nonzero h does not help the normal mode model, as it already has EVPA larger than that of the late-phase points.

The $i \approx 60^\circ$ orthogonal RVM model has the minimum χ^2, but there is a major peculiarity: the radio peak appears when the associated magnetic pole sweeps $|\beta| = |i - \theta| = 63^\circ$ from the Earth line of sight, while the opposite pole, sweeping 3° away at $\phi = 0.44$, shows no radio emission. In contrast, the other two models have large but less extreme $\beta \approx -29^\circ$. Of these, the normal mode model has the radio pulse leading the radio axis by a substantial 49°, while the orthogonal solution would have the radio pulse trailing the magnetic axis. Thus, no solution is ideal, and all require a very large, partly filled radio beam. Additional significant X-ray EVPAs would certainly help the model discrimination, as would more late-phase radio measurements.

5. Conclusions

In sum, the CXO-measured X-ray morphology of the inner PWN does constrain the 3D spin axis and helps select between otherwise viable RVM fits to the PSR B1509−58 radio polarization. With IXPE we also extract a single phase bin of pulsar X-ray polarization. This is plausibly interpreted as an extension of the radio polarization sweep, but with only one significant bin, it its difficult to make detailed model tests. Further IXPE observations could promote 2–3 more bins to 3σ significance but would probably require ∼2 Ms of additional exposure.

We conclude by noting that the rich polarization structure of the MSH $15-5^2$ PWN reflects the interplay of axisymetric pulsar outflow and complex, possibly unstable interaction with the surrounding SNR. Although, unlike the Crab and Vela PWNe, toroidal symmetry does not dominate the polarization pattern, the polarization degree of MSH $15-5^2$ is similar to that found earlier by IXPE for the Crab and Vela: polarization is very high in parts of the hard spectrum emission regions, approaching the maximum PD allowed for synchrotron emission (Xie et al. 2022). This suggests that these portions of the PWN contain uniform fields with little turbulence. On the other hand, the base of the jet, which may be reaccelerating particles, has a low polarization and complex field geometry. It seems that if diffusive shock acceleration energizes the PWN particles, then much of the radiation comes from uniform field zones separate from the acceleration sites. Alternatively, a lower-turbulence mechanism, possibly associated with magnetic reconnection, may be involved. Full mapping of the field geometry requires higher resolution and sensitivity than IXPE can provide. But even the present data provide a visually striking polarization map of the Cosmic Hand's fields and some important challenges to MHD PWN models.

Acknowledgments

The Imaging X-ray Polarimetry Explorer (IXPE) is a joint US and Italian mission. The US contribution is supported by the National Aeronautics and Space Administration (NASA) and led and managed by its Marshall Space Flight Center (MSFC), with industry partner Ball Aerospace (contract NNM15AA18C). The Italian contribution is supported by the Italian Space Agency (Agenzia Spaziale Italiana, ASI) through contract ASI-OHBI-2017-12-I.0, agreements ASI-INAF-2017-12-H0 and ASI-INFN-2017.13-H0, and its Space Science Data Center (SSDC) with agreements ASI-INAF-2022-14-HH.0 and ASI-INFN 2021-43-HH.0, and by the Istituto Nazionale di Astrofisica (INAF) and the Istituto Nazionale di Fisica Nucleare (INFN) in Italy. This research used data products provided by the IXPE Team (MSFC, SSDC, INAF, and INFN) and distributed with additional software tools by the High Energy Astrophysics Science Archive Research Center (HEASARC), at NASA Goddard Space Flight Center (GSFC). Funding for this work was provided in part by contract NNM17AA26C from the MSFC to Stanford and 80MSFC17C0012 to MIT in support of the IXPE project. Support for this work was provided in part by NASA through the Smithsonian Astrophysical Observatory (SAO)contract SV3-73016 to MIT for support of the Chandra X-Ray Center (CXC), which is operated by SAO for and on behalf of NASA under contract NAS8-03060. C.-Y.N. and Y.-J.Y. are supported by a GRF grant of the Hong Kong Government

under HKU 17305419. N.B. was supported by the INAF MiniGrant "PWNnumpol—Numerical Studies of Pulsar Wind Nebulae in The Light of IXPE."

Facilities: ATCA, CXO, IXPE.

ORCID iDs

Roger W. Romani https://orcid.org/0000-0001-6711-3286
Josephine Wong https://orcid.org/0000-0001-6395-2066
Niccoló Di Lalla https://orcid.org/0000-0002-7574-1298
Nicola Omodei https://orcid.org/0000-0002-5448-7577
Fei Xie https://orcid.org/0000-0002-0105-5826
C.-Y. Ng https://orcid.org/0000-0002-5847-2612
Riccardo Ferrazzoli https://orcid.org/0000-0003-1074-8605
Alessandro Di Marco https://orcid.org/0000-0003-0331-3259
Niccoló Bucciantini https://orcid.org/0000-0002-8848-1392
Maura Pilia https://orcid.org/0000-0001-7397-8091
Patrick Slane https://orcid.org/0000-0002-6986-6756
Martin C. Weisskopf https://orcid.org/0000-0002-5270-4240
Simon Johnston https://orcid.org/0000-0002-7122-4963
Marta Burgay https://orcid.org/0000-0002-8265-4344
Deng Wei https://orcid.org/0000-0002-9370-4079
Yi-Jung Yang https://orcid.org/0000-0001-9108-573X
Shumeng Zhang https://orcid.org/0000-0002-0007-7214
Lucio A. Antonelli https://orcid.org/0000-0002-5037-9034
Matteo Bachetti https://orcid.org/0000-0002-4576-9337
Luca Baldini https://orcid.org/0000-0002-9785-7726
Wayne H. Baumgartner https://orcid.org/0000-0002-5106-0463
Ronaldo Bellazzini https://orcid.org/0000-0002-2469-7063
Stefano Bianchi https://orcid.org/0000-0002-4622-4240
Stephen D. Bongiorno https://orcid.org/0000-0002-0901-2097
Raffaella Bonino https://orcid.org/0000-0002-4264-1215
Alessandro Brez https://orcid.org/0000-0002-9460-1821
Fiamma Capitanio https://orcid.org/0000-0002-6384-3027
Simone Castellano https://orcid.org/0000-0003-1111-4292
Elisabetta Cavazzuti https://orcid.org/0000-0001-7150-9638
Chien-Ting Chen https://orcid.org/0000-0002-4945-5079
Nicoló Cibrario https://orcid.org/0000-0003-3842-4493
Stefano Ciprini https://orcid.org/0000-0002-0712-2479
Enrico Costa https://orcid.org/0000-0003-4925-8523
Alessandra De Rosa https://orcid.org/0000-0001-5668-6863
Ettore Del Monte https://orcid.org/0000-0002-3013-6334
Immacolata Donnarumma https://orcid.org/0000-0002-4700-4549
Victor Doroshenko https://orcid.org/0000-0001-8162-1105
Michal Dovčiak https://orcid.org/0000-0003-0079-1239
Steven R. Ehlert https://orcid.org/0000-0003-4420-2838
Teruaki Enoto https://orcid.org/0000-0003-1244-3100
Yuri Evangelista https://orcid.org/0000-0001-6096-6710
Sergio Fabiani https://orcid.org/0000-0003-1533-0283
Javier A. Garcia https://orcid.org/0000-0003-3828-2448
Shuichi Gunji https://orcid.org/0000-0002-5881-2445
Jeremy Heyl https://orcid.org/0000-0001-9739-367X
Wataru Iwakiri https://orcid.org/0000-0002-0207-9010
Ioannis Liodakis https://orcid.org/0000-0001-9200-4006
Philip Kaaret https://orcid.org/0000-0002-3638-0637
Vladimir Karas https://orcid.org/0000-0002-5760-0459
Dawoon E. Kim https://orcid.org/0000-0001-5717-3736
Jeffery J. Kolodziejczak https://orcid.org/0000-0002-0110-6136
Henric Krawczynski https://orcid.org/0000-0002-1084-6507
Fabio La Monaca https://orcid.org/0000-0001-8916-4156
Luca Latronico https://orcid.org/0000-0002-0984-1856
Simone Maldera https://orcid.org/0000-0002-0698-4421
Alberto Manfreda https://orcid.org/0000-0002-0998-4953
Frédéric Marin https://orcid.org/0000-0003-4952-0835
Andrea Marinucci https://orcid.org/0000-0002-2055-4946
Alan P. Marscher https://orcid.org/0000-0001-7396-3332
Herman L. Marshall https://orcid.org/0000-0002-6492-1293
Francesco Massaro https://orcid.org/0000-0002-1704-9850
Giorgio Matt https://orcid.org/0000-0002-2152-0916
Riccardo Middei https://orcid.org/0000-0001-9815-9092
Tsunefumi Mizuno https://orcid.org/0000-0001-7263-0296
Fabio Muleri https://orcid.org/0000-0003-3331-3794
Michela Negro https://orcid.org/0000-0002-6548-5622
Stephen L. O'Dell https://orcid.org/0000-0002-1868-8056
Chiara Oppedisano https://orcid.org/0000-0001-6194-4601
Luigi Pacciani https://orcid.org/0000-0001-6897-5996
Alessandro Papitto https://orcid.org/0000-0001-6289-7413
George G. Pavlov https://orcid.org/0000-0002-7481-5259
Melissa Pesce-Rollins https://orcid.org/0000-0003-1790-8018
Pierre-Olivier Petrucci https://orcid.org/0000-0001-6061-3480
Andrea Possenti https://orcid.org/0000-0001-5902-3731
Juri Poutanen https://orcid.org/0000-0002-0983-0049
Brian D. Ramsey https://orcid.org/0000-0003-1548-1524
John Rankin https://orcid.org/0000-0002-9774-0560
Ajay Ratheesh https://orcid.org/0000-0003-0411-4243
Oliver J. Roberts https://orcid.org/0000-0002-7150-9061
Carmelo Sgró https://orcid.org/0000-0001-5676-6214
Paolo Soffitta https://orcid.org/0000-0001-8916-4156
Gloria Spandre https://orcid.org/0000-0003-0802-3453
Douglas A. Swartz https://orcid.org/0000-0002-2954-4461
Toru Tamagawa https://orcid.org/0000-0002-8801-6263
Fabrizio Tavecchio https://orcid.org/0000-0003-0256-0995
Roberto Taverna https://orcid.org/0000-0002-1768-618X
Allyn F. Tennant https://orcid.org/0000-0002-9443-6774
Nicholas E. Thomas https://orcid.org/0000-0003-0411-4606
Francesco Tombesi https://orcid.org/0000-0002-6562-8654
Alessio Trois https://orcid.org/0000-0002-3180-6002
Sergey Tsygankov https://orcid.org/0000-0002-9679-0793
Roberto Turolla https://orcid.org/0000-0003-3977-8760
Jacco Vink https://orcid.org/0000-0002-4708-4219
Kinwah Wu https://orcid.org/0000-0002-7568-8765
Silvia Zane https://orcid.org/0000-0001-5326-880X

References

Abdo, A. A., Ackermann, M., Ajello, M., et al. 2010, ApJ, 714, 927
Aharonian, F., Akhperjanian, A. G., Aye, K. M., et al. 2005, A&A, 435, L17
An, H., Madsen, K. K., Reynolds, S. P., et al. 2014, ApJ, 793, 90
Baldini, L., Bucciantini, N., Lalla, N. D., et al. 2022, SoftX, 19, 101194
Brazier, K. T. S., & Becker, W. 1997, MNRAS, 284, 335
Bucciantini, N., Di Lalla, N., Romani, R. W. R., et al. 2023, A&A, 672, A66
Caswell, J. L., Milne, D. K., & Wellington, K. J. 1981, MNRAS, 195, 89
Crawford, F., Manchester, R. N., & Kaspi, V. M. 2001, AJ, 122, 2001

Cusumano, G., Mineo, T., Massaro, E., et al. 2001, A&A, 375, 397
de Plaa, J., Kuiper, L., & Hermsen, W. 2003, A&A, 400, 1013
DeLaney, T., Gaensler, B. M., Arons, J., & Pivovaroff, M. J. 2006, ApJ, 640, 929
Di Marco, A., Soffitta, P., Costa, E., et al. 2023, AJ, 165, 143
Everett, J. E., & Weisberg, J. M. 2001, ApJ, 553, 341
Gaensler, B. M., Arons, J., Kaspi, V. M., et al. 2002, ApJ, 569, 878
Hu, C.-P., Ng, C. Y., Takata, J., Shannon, R. M., & Johnston, S. 2017, ApJ, 838, 156
Johnston, S., Hobbs, G., Vigeland, S., et al. 2005, MNRAS, 364, 1397
Johnston, S., & Weisberg, J. M. 2006, MNRAS, 368, 1856
Kawai, N., Okayasu, R., Brinkmann, W., et al. 1991, ApJL, 383, L65
Komissarov, S. S., & Lyubarsky, Y. E. 2003, MNRAS, 344, L93
Leung, W. Y., & Ng, C. Y. 2016, in Supernova Remnants: An Odyssey in Space after Stellar Death, 53
Manchester, R. N., Tuohy, I. R., & Damico, N. 1982, ApJL, 262, L31
Nasa High Energy Astrophysics Science Archive Research Center (HEASARC), 2014 HEAsoft: Unified Release of FTOOLS and XANADU, Astrophysics Source Code Library, ascl:1408.004
Ng, C. Y., & Romani, R. W. 2008, ApJ, 673, 411
Poutanen, J. 2020, A&A, 641, A166
Radhakrishnan, V., & Cooke, D. J. 1969, ApL, 3, 225
Rookyard, S. C., Weltevrede, P., & Johnston, S. 2015a, MNRAS, 446, 3356
Rookyard, S. C., Weltevrede, P., & Johnston, S. 2015b, MNRAS, 446, 3367
Seward, F. D., & Harnden, F. R., Jr. 1982, ApJL, 256, L45
Wagner, S. J., & Seifert, W. 2000, in ASP Conf. Ser. 202, IAU Colloq. 177: Pulsar Astronomy—2000 and Beyond, ed. M. Kramer, N. Wex, & R. Wielebinski (San Francisco, CA: ASP), 315
Weisskopf, M. C., Soffitta, P., Baldini, L., et al. 2022, JATIS, 8, 026002
Wong, J., Romani, R. W., & Dinsmore, J. T. 2023, ApJ, 953, 28
Xie, F., Di Marco, A., La Monaca, F., et al. 2022, Natur, 612, 658
Yatsu, Y., Kawai, N., Shibata, S., & Brinkmann, W. 2009, PASJ, 61, 129